Transition Edge Sensors for DC Operation and Low Magnetic Field Sensitivity

De Wit, M.; Gottardi, L.; Nagayoshi, K.; Taralli, E.; Vaccaro, D.; Ravensberg, K.; Bruijn, M. P.; Van Der Kuur, J.; Gao, J. R.; Den Herder, J. W.A.

DOI
10.1109/TASC.2024.3521900

Publication date
2025

Document Version
Final published version

Published in
IEEE Transactions on Applied Superconductivity

Transition Edge Sensors for DC Operation and Low Magnetic Field Sensitivity

M. de Wit, L. Gottardi, K. Nagayoshi, E. Taralli, D. Vaccaro, K. Ravensberg, M.P. Bruijn, J. van der Kuur, J.R. Gao, and J.W.A. den Herder

***Abstract*—The X-ray Integral Field Unit (X-IFU) is an imaging spectrometer based on a large array of Transition Edge Sensors (TES) measured using Time Domain Multiplexing (TDM). For the development of a backup detector array, we have designed and realized a cryogenic test setup capable of measuring 9 detectors in a single cooldown under DC bias. We have used this setup to study a small selection of low aspect ratio TES designs, intended to have a low normal resistance suitable for TDM readout. In this work we show how the different designs are affected by magnetic fields. We do this by presenting the impact on the transition shape, detector integrated Noise Equivalent Power (NEP), and sensitivity of the energy scale calibration. We find, in agreement with previous studies, that reducing the width of the TES bilayer greatly improves the detector resilience to magnetic fields, potentially by several orders of magnitude.**

***Index Terms*—Superconducting photodetectors, X-ray detectors, superconducting device noise.**

I. Introduction

THE X-ray Integral Field Unit (X-IFU) is an imaging X-ray spectrometer to be mounted on the European Space Agency's (ESA) Advanced Telescope for High-ENergy Astrophysics (Athena). X-IFU will consist of an array of 1504 Transition Edge Sensor (TES) microcalorimeters. The TES are optimized for the detection of photons with energies ranging from 0.2 to 12 keV with an energy resolution below 4.0 eV at 7 keV [1]. At SRON we have developed state-of-the-art detector arrays to be used as a backup for the X-IFU instrument, with the baseline array being delivered by NASA Goddard Space and Flight Center (GSFC) [2]. Apart from their applications in space, TES also show great potential for earthbound applications such as diagnostics for fusion reactors and to study astrophysical plasmas in electron beam ion traps (EBITs) [3], [4].

One of the key selling points for using Transition Edge Sensors is their exquisite sensitivity, allowing for high energy resolving power over a wide range of photon energies. This sensitivity is achieved by utilizing the sharp relation between resistance and temperature within the phase transition of a superconductor. To make a TES for X-ray detection a thin superconducting strip is strongly thermally coupled to an X-ray absorber and weakly thermally coupled to the thermal bath, i.e. by use of a thin Si_3N_4 membrane. The superconducting strip is typically made of a normal-metal/superconductor bilayer to allow careful tuning of the critical temperature. When the TES is operated within this transition, the minute energy of a photon being absorbed increases the temperature of the TES, which in turn induces a large change in the resistance. Precise measurements of the change in TES resistance or current can be used to reconstruct the energy of the photon with high accuracy. Further details of TES operation and physics are given elsewhere [5], [6], [7].

The baseline readout technology for X-IFU used to be based on Frequency Domain Multiplexing (FDM) [8]. In this scheme detectors are operated using AC bias at several frequencies between 1 to 5 MHz. Previous work has shown that for TES that are operated under AC bias the weak-link effect is the main source of noise [9], [10]. This problem can be minimized by increasing the normal resistance (R_n) of the TES by using bilayers of thin layer thickness and high aspect ratio [11]. However, in early 2020 the baseline readout technology for X-IFU was changed from FDM to Time Division Multiplexing (TDM). In TDM detectors are operated using a DC bias with rapid switching between multiple detectors in a single readout chain [12]. In order to have good impedance matching between the TES and the TDM circuit low R_n TES are optimal. Therefore, the change of the read-out technology has a significant impact on our development of the backup detector array, for which we have to transition from high to low R_n devices.

In this paper we discuss the results of an investigation of different low R_n TES designs. Instead of copying the design of the NASA GSFC developed TDM detectors, we have performed an independent investigation in order to verify previous findings and gain experience and complementary knowledge. We describe the setup that we developed to operate our detectors

Received 25 September 2024; revised 11 December 2024; accepted 13 December 2024. Date of publication 24 December 2024; date of current version 13 January 2025. This work was supported in part by the European Space Agency through ESA CTP under Grant 4000130346/20/NL/BW/os and in part by NWO, The Dutch Research Council through SRON. *(Corresponding author: M. de Wit.)*

M. de Wit, L. Gottardi, K. Nagayoshi, E. Taralli, D. Vaccaro, K. Ravensberg, and M.P. Bruijn are with the NWO-I/SRON Netherlands Institute for Space Research, 2333 CA Leiden, The Netherlands (e-mail: m.de.wit@sron.nl).

J. van der Kuur is with the NWO-I/SRON Netherlands Institute for Space Research, 2333 CA Leiden, The Netherlands, and also with the NWO-I/SRON Netherlands Institute for Space Research, 9747 AD Groningen, The Netherlands.

J.R. Gao is with the NWO-I/SRON Netherlands Institute for Space Research, 2333 CA Leiden, The Netherlands, and also with the Optics Research Group, Department of Imaging Physics, Delft University of Technology, 2628 CH Delft, The Netherlands.

J.W.A. den Herder is with the NWO-I/SRON Netherlands Institute for Space Research, 2333 CA Leiden, The Netherlands, and also with the Anton Pannekoek Institute, University of Amsterdam, 1098 XH Amsterdam, The Netherlands.

Color versions of one or more figures in this article are available at https://doi.org/10.1109/TASC.2024.3521900.

Digital Object Identifier 10.1109/TASC.2024.3521900

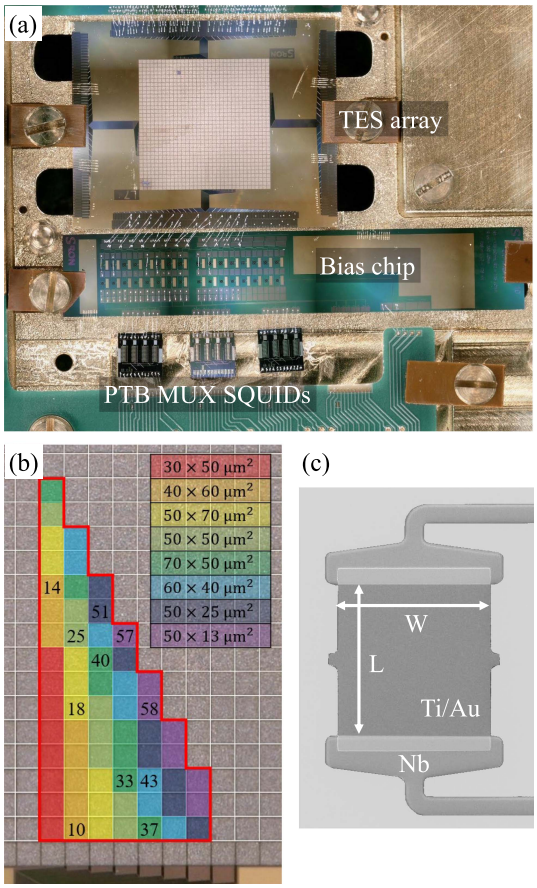

Fig. 1. (a) Photograph of the TES array, the bias chip containing the Nyquist inductors and shunt resistors, and SQMUX chips (3 out of 4 installed). (b) Zoom in on the TES array with the numbers indicating the measured detectors. The colors indicate different designs according to the legend. (c) Photograph of an example TES, with the arrows indication the definition of the length L and width W.

under DC bias, a deviation from our decade long experience developing AC biased readout systems. We discuss the relevant properties of our detector array, and how this varies from the approach taken by NASA GSFC. Regarding the identification of the optimal design, we focus in this paper on how to maximize the pixel resilience against magnetic fields. As the presence of magnetic fields can reduce the intrinsic pixel performance and affect the energy scale calibration, low magnetic field sensitivities are strongly preferred. This is particularly important for TES-based instruments that will be operated in space due to the stringent limitations on both the mass and volume of potential magnetic shielding, and the inevitable stray fields resulting from the ADR-based cooling chains. The results of this study can be of interest for both Athena's X-IFU as well as other space-borne TES-based X-ray instruments such as the Line Emission Mapper (LEM) [13] and the Hot Universe Baryon Surveyor (HUBS) [14].

II. Cryogenic Setup and TES Array

Detector characterization at SRON is generally done using our heritage FDM readout systems. However, these are ill-suited for the measurement of low R_n detectors due to the large weak-link effect. Therefore, we have developed a new setup for DC bias operation which allows in a single cooldown the individual measurement of several detectors. A photograph of this setup is visible in 1(a). Each TES is connected in parallel to a shunt resistor ($R_{sh} = 270$ µΩ), and in series with a Nyquist inductor ($L_{NY} = 130$ or 320 nH, both allowing operation in the low inductance limit) and the input coil of the Series SQUID Array (SSA). A common line is used to DC voltage bias all the TES simultaneously. The SSA are located in groups of four on PTB single stage SQUID multiplexers (SQMUX). During these tests, 3 SQMUX were installed, with a total of 9 fully functional channels. Superconducting switches are used to select the active channel on each SQMUX, hereby allowing the individual readout of each TES. The setup is mounted from a kevlar vibration isolation [15] at the mixing chamber of a Leiden Cryogenics dilution refrigerator. Magnetic shielding is achieved using a niobium shield at the cryogenic setup and a mu-metal shield at room temperature around the cooler. An 55Fe X-ray source is mounted in the snout of the niobium shield to expose the TES array to 5.9 keV photons. A superconducting coil is used to apply small magnetic fields perpendicular to the TES bilayers. All presented data was measured at a bath temperature of 50 mK.

To study the performance of different pixel designs, we have fabricated a mixed kilo-pixel array containing devices with varying bilayer dimensions ($L \times W$ µ^{2}m). A picture of the array is visible in Fig. 1(b), in which the different colors indicate different bilayer dimensions. The available designs can be read from the legend. A photograph of an example TES is visible in Fig. 1(c). The TES are designed to be suitable as backup for X-IFU. They consist of a Ti/Au bilayer with a sheet resistance of $\sim 14\,\mathrm{m\Omega/\square}$. In contrast to the detectors at NASA GSFC, we do not use normal metal banks at the edges of the bilayer, leading to a higher final device resistance. This results in detectors with R_n ranging from 8.4 to 53 mΩ. The detectors have a mean critical temperature (T_C) of 90 mK, with a small increase in T_C for short detectors and a decrease for narrow devices resulting from the longitudinal and lateral inverse proximity effect [11], [16]. The bilayers are coupled to X-ray absorbers with an area of 270×270 µ^{2}m and a 5 µm gap between neighbouring absorbers, creating a total pixel pitch of 275 µm. The electroplated absorbers are made of 2.0 um Au and 3.5 um Bi, leading to a calculated heat capacity of 90 pJ/K at T_C. The bilayers are grown on a 190 µm^2 Si_3N_4 membrane with a thickness of 0.5 µm. The thermal conductance G_{bath} is dominated by radiative phonon transport and therefore proportional to the perimeter of the bilayer plus supporting stems with absolute values ranging from ~50 to 80 pW/K for the different designs. Note that we have only investigated the intrinsic detector properties. Properties resulting from the detector-readout interplay, such as the slew-rate, have not been assessed.

III. Measurements

In order to study the impact of the bilayer design on pixel, we have characterized the different detector designs at different applied magnetic fields. In particular, we have looked for

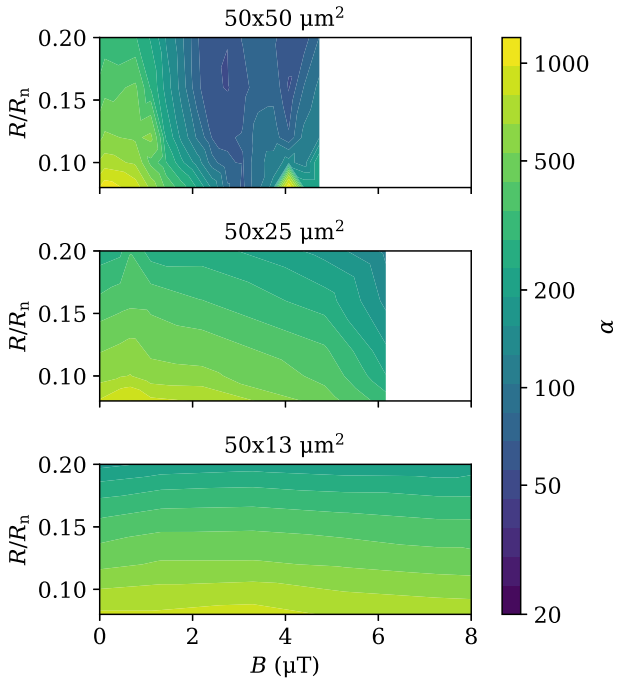

Fig. 2. Contour plot of alpha versus magnetic field and bias point R/R_n for three devices of $L = 50$ μm and varying width.

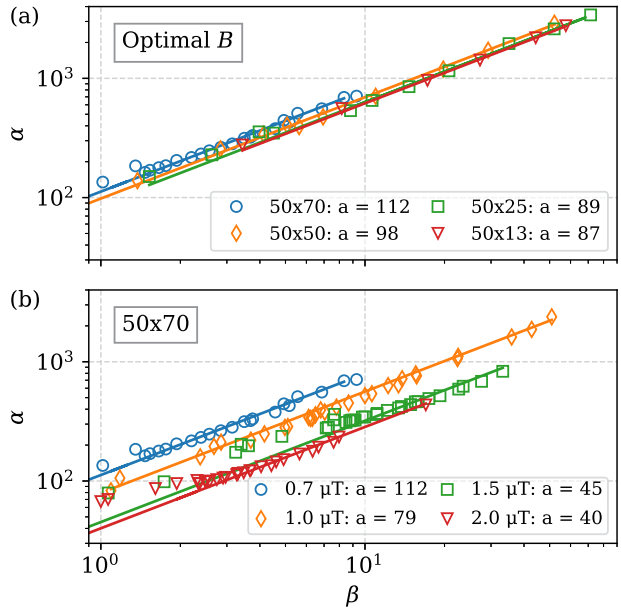

Fig. 3. (a) Measured α versus β for four devices of varying width, measured at the optimal cancelling field for each detector. (b) Measured α versus β for the 50×70 device measured at several different magnetic fields. Solid lines are fits to an emperical power law model $\alpha = a\beta^b$ with fixed exponent $b = 0.85$. Fitted values for a are given in the figure legends.

differences in the transition curve such as the logarithmic sensitivity with respect to temperature and current, given by $\alpha = \frac{R}{T}\frac{dT}{dR}\big|_{T_0}$ and $\beta = \frac{I}{T}\frac{dT}{dI}\big|_{I_0}$ respectively. α and β are obtained using the standard complex impedance method [17], [18]. Contour plots of the measured α are shown in Fig. 2 as a function of magnetic field and bias point R/R_n. The different subfigures show a subset of three different designs of length 50 μm and varying width. β is not shown here, but follows a similar trend as α. At constant magnetic field all devices show a smoothly evolving α as a function of bias point, contrary to what is observed when operating low R_n detectors under AC bias [11]. However, large oscillations are visible as the magnetic field is varied, in particular for the widest devices. As the width of the bilayer is reduced, the oscillation period increases such that small variations in the magnetic field no longer affect the transition shape. This is in agreement with previous observations both under DC and AC bias [19], [20].

A high ratio between α and β is a good first indication for a good energy resolution. Previous work has shown that for very short bilayers ($L \lesssim 40$ μm) there is a degradation of α/β, observed both under AC and DC bias [21], [22]. In Fig. 3(a) we show α versus β for four devices measured at the optimal cancelling field (defined as the field required to null the field at the TES with zero TES current). The solid lines are fits to an emperical power law $\alpha = a\beta^b$ with fixed exponent $b = 0.85$ for all curves (chosen as the best fitting global parameter). There is no major effect of the device width on α/β, definitely not of the same magnitude as observed for the bilayer length. Yet, one could see a minor enhancement of the ratio for the wider devices. At best this enhancement seems to be about 20%. However, due to too scarce sampling of magnetic fields and bias points for all devices we are hesitant to draw hard conclusions. Note that the effect could also be caused by different R_n due to the changing bilayer aspect ratio.

A much bigger effect is seen when looking at α/β away from the optimal field, as demonstrated in Fig. 3(b) where we show data from the 50×70 device at a few field values. α/β has a clear maximum when the residual field at the TES is best cancelled and rapidly decreases as sub-optimal fields are applied.

There is a correlation between the regions of high α and good predicted energy resolution for the pixels. We demonstrate this in Fig. 4, where we show for the same devices as those from Fig. 2 the integrated Noise Equivalent Power (NEP) measured under similar conditions. In particular for the 50×50 device a direct comparison for equal bias points can be made. While all devices show integrated NEP well below 2eV, for the 50×50 devices achieving this required significant fine tuning of the magnetic field. The magnetic field region showing best performance is extremely narrow, below 0.5 μT. Wider devices require even more stringent tuning, down to 0.1–0.2 μT. The 50×25 device performs already significantly better, showing a much larger optimal region with first signs of degradation of the predicted resolution appearing above 2 μT. Finally, the 50×13 device stays below 2eV over the full measured range of magnetic fields.

A second effect of the magnetic fields is not a direct degradation of the detector properties, but instead that the magnetic field changes the gain of the detector and thereby the energy scale calibration. Temporal drifts of the energy scale function lead to a worsened energy resolution as well as systematic errors in the absolute energy of the measured photons [23]. Here we have measured the impact on the energy scale calibration by

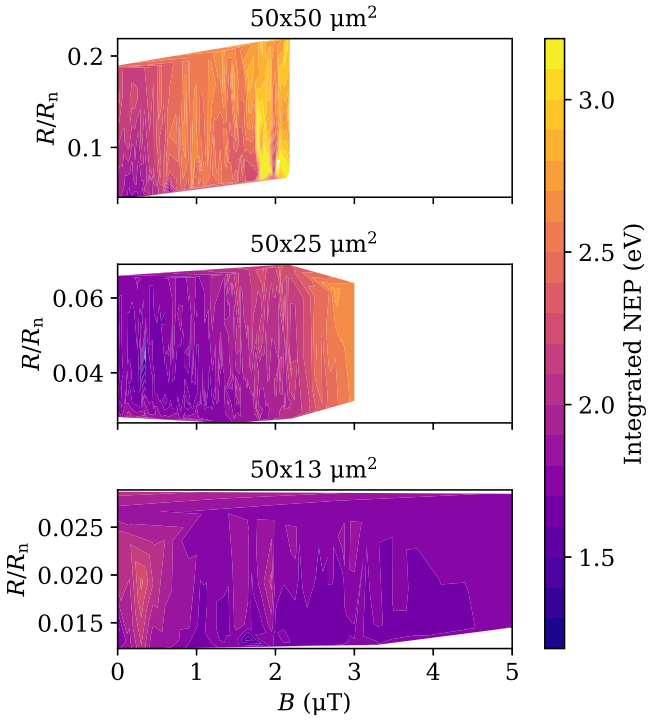

Fig. 4. Contour plot of integrated NEP versus magnetic field and bias point for three devices of varying width. Note that the reason for the low R/Rn shown for the 50×25 and 50×13 devices is not driven by detector properties, but results from the automated measurement where a constant bias voltage range was used, leading to lower R for the higher R_n and lower G devices.

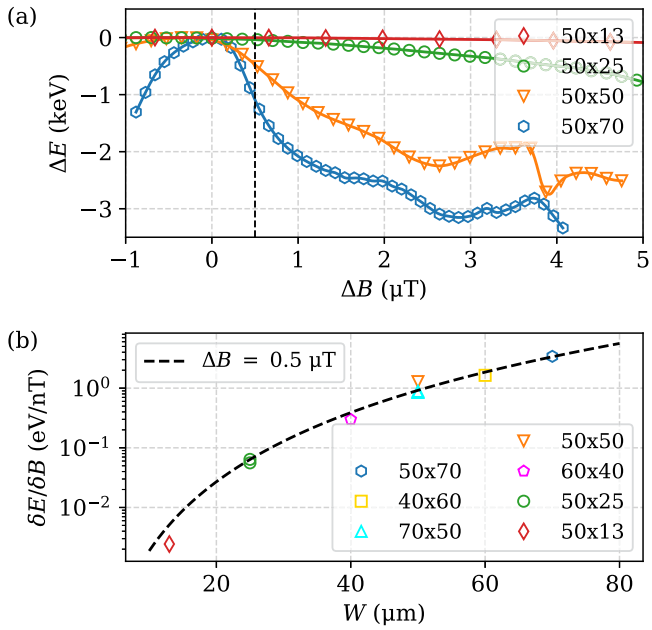

Fig. 5. top figure: ΔE (shift with respect to 5.9 keV) versus ΔB (applied magnetic field relative to the optimal cancelling field). Bottom figure: local derivative of the top figure, evaluated at $\Delta B = 0.5\,\mu$T. The dashed line is a fit to an empirical power law model, serving as a guide to the eye.

measuring for each detector at several magnetic field values a few hundred photons from the Mn-Kα complex. Details of the measurement method are given by Vaccaro et al. [24]. In Fig. 5(a) we show the measured shift of the calibrated energy away from the 5.9 keV of Mn-Kα versus the shift in magnetic field away from the optimal cancelling field (at which the detector responsivity is largest). For clarity we only show a subset of the measured detectors in this figure.

We evaluate the sensitivity by taking the local derivative $(\delta B/\delta E)$ at a constant magnetic field shift of 0.5 μT, indicated by the black dashed line. The main driver for the sensitivity is the width, as shown in Fig. 5(b) where we show the local derivative versus the bilayer width (W). The dashed line is a fit to an empirical power law model, and only serves as a guide to the eye. The precise relation between $\delta B/\delta E$ and W changes depending on the field at which it is evaluated. Note that our choice to evaluate the sensitivity at $\Delta B = 0.5$ μT is arbitrary to a certain degree. For any specific case, it should match the maximum expected gradient across the array which cannot by cancelled by an external field source, i.e. a Helmholtz coil. The strong relation between the sensitivity and the device width originates from a few contributions. First of all, the shape of ΔE versus ΔB is related to the Fraunhofer-like pattern of the detector $I_C(B)$ resulting from the weak-link effect. The oscillation period of this pattern inversely depends on the area of the weak-link, and thus increases for narrow detectors. Additionally, non-uniformity of the current distribution, in particular a current distribution that peaks in the center of the bilayer as can be expected from narrow devices, broadens the central maximum of the pattern. Another contribution is that the current in the TES creates a self-magnetic field. The magnitude of this self-field decreases for devices with high R_n or low G_{bath}, for which lower TES currents are needed. This effect is expected to be modest compared to the former.

IV. Conclusion

In order to characterize the behaviour of different TES designs when operated using TDM, we have developed a new test setup capable of testing 9 detectors in a single cooldown using a DC voltage bias. We have used this setup to study a number of different low normal resistance designs. Here we have reported in particular on the relation between the TES design and the sensitivity to magnetic field. Magnetic fields affect the transition shape as well as the detector responsivity and energy resolution, as demonstrated via measurements of α, β, and integrated NEP at various magnetic fields. Reducing the width of the detectors greatly mitigates the impact of magnetic fields on the detector properties. Additionally, we have shown that the susceptibility to magnetic fields of the energy scale calibration can be reduced by several orders of magnitude. While there are certainly other considerations aside from magnetic field sensitivity when selecting the best bilayer design, the usage of narrow TES would greatly relax the requirements on magnetic field shielding and would aid in the accurate calibration of the absolute photon energies. The results agree with earlier observations under AC and DC biasing, and provide further affirmation for the recent decision to change the X-IFU TES design from 50×50 to $50 \times 30\,\mu m^2$ as reported by Wakeham et al. [20].

REFERENCES

[1] D. Barret et al., "The athena X-ray integral field unit: A consolidated design for the system requirement review of the preliminary definition phase," *Exp. Astron.*, vol. 55, no. 2, pp. 373–426, 2023.

[2] S. J. Smith et al., "Performance of a broad-band, high-resolution, transition-edge sensor spectrometer for X-ray astrophysics," *IEEE Trans. Appl. Supercond.*, vol. 31, no. 5, Aug. 2021, Art. no. 2100806.

[3] F. Porter et al., "The XRS microcalorimeter spectrometer at the livermore electron beam ion trap," *Can. J. Phys.*, vol. 86, no. 1, pp. 231–240, 2008.

[4] P. Szypryt et al., "A transition-edge sensor-based X-ray spectrometer for the study of highly charged ions at the national institute of standards and technology electron beam ion trap," *Rev. Sci. Instrum.*, vol. 90, no. 12, 2019.

[5] K. D. Irwin and G. C. Hilton, "Transition-edge sensors," *Cryogenic Particle Detection, Topics Appl. Phys.*, vol. 99, pp. 63–152, 2005.

[6] J. N. Ullom and D. A. Bennett, "Review of superconducting transition-edge sensors for X-ray and gamma-ray spectroscopy," *Supercond. Sci. Technol.*, vol. 28, no. 8, 2015, Art. no. 084003.

[7] L. Gottardi and K. Nagayashi, "A review of X-ray microcalorimeters based on superconducting transition edge sensors for astrophysics and particle physics," *Appl. Sci.*, vol. 11, no. 9, 2021, Art. no. 3793.

[8] D. Vaccaro et al., "Developments on frequency domain multiplexing readout for large arrays of transition-edge sensor X-ray micro-calorimeters," *J. Low Temp. Phys.*, vol. 216, pp. 21–28, 2024.

[9] L. Gottardi et al., "Josephson effects in frequency-domain multiplexed tes microcalorimeters and bolometers," *J. Low Temp. Phys.*, vol. 193, pp. 209–216, 2018.

[10] L. Gottardi, M. de Wit, E. Taralli, K. Nagayashi, and A. Kozorezov, "Voltage fluctuations in AC biased superconducting transition-edge sensors," *Phys. Rev. Lett.*, vol. 126, no. 21, Art. no. 217001, 2021.

[11] M. De Wit et al., "High aspect ratio transition edge sensors for X-ray spectrometry," *J. Appl. Phys.*, vol. 128, no. 22, 2020.

[12] W. B. Doriese, R. Kraft, C. Kilbourne, S. Bandler, and S. Smith, "Time-division SQUID multiplexed readout for athena X-IFU and the LEM microcalorimeter spectrometer," *AAS/High Energy Astrophys. Division*, vol. 55, no. 4, pp. 110–15, 2023.

[13] R. Kraft et al., "The line emission mapper (LEM) probe mission concept," *Proc. SPIE*, vol. 13093, pp. 656–709, 2024.

[14] W. Cui et al., "Hubs: A dedicated hot circumgalactic medium explorer," *Proc. SPIE*, vol. 11444, pp. 470–481, 2020.

[15] L. Gottardi et al., "A six-degree-of-freedom micro-vibration acoustic isolator for low-temperature radiation detectors based on superconducting transition-edge sensors," *Rev. Sci. Instrum.*, vol. 90, no. 5, 2019.

[16] J. E. Sadleir, S. J. Smith, S. R. Bandler, J. A. Chervenak, and J. R. Clem, "Longitudinal proximity effects in superconducting transition-edge sensors," *Phys. Rev. Lett.*, vol. 104, no. 4, 2010, Art. no. 047003.

[17] M. A. Lindeman et al., "Impedance measurements and modeling of a transition-edge-sensor calorimeter," *Rev. Sci. Instrum.*, vol. 75, no. 5, pp. 1283–1289, 2004.

[18] E. Taralli et al., "Complex impedance of TESs under AC bias using FDM readout system," *AIP Adv.*, vol. 9, no. 4, 2019.

[19] M. de Wit et al., "Performance of the SRON Ti/Au transition edge sensor X-ray calorimeters," *Proc. SPIE*, vol. 12181, pp. 583–594, 2022.

[20] N. Wakeham et al., "Refinement of transition-edge sensor dimensions for the X-ray integral field unit on ATHENA," *IEEE Trans. Appl. Supercond.*, vol. 33, no. 5, Aug. 2023, Art. no. 2100506.

[21] S. J. Smith et al., "Small pitch transition-edge sensors with broadband high spectral resolution for solar physics," *J. Low Temp. Phys.*, vol. 167, no. 3/4, pp. 168–175, 2012.

[22] E. Taralli et al., "Small size transition-edge sensors for future X-ray applications," *J. Low Temp. Phys.*, vol. 209, no. 3, pp. 256–262, 2022.

[23] S. J. Smith et al., "Correcting gain drift in TES detectors for future X-ray satellite missions," *IEEE Trans. Appl. Supercond.*, vol. 33, no. 5, Aug. 2023, Art. no. 2101006.

[24] D. Vaccaro et al., "Susceptibility study of TES micro-calorimeters for X-ray spectroscopy under FDM readout," *J. Low Temp. Phys.*, vol. 209, no. 3, pp. 562–569, 2022.